

Document downloaded from:

<http://hdl.handle.net/10251/199521>

This paper must be cited as:

Fernández-Cavero, V.; Pons Llinares, J.; Duque-Perez, O.; Morinigo-Sotelo, D. (2021). Detection and quantification of bar breakage harmonics evolutions in inverter-fed motors through the dragon transform. *ISA Transactions*. 109:352-367.  
<https://doi.org/10.1016/j.isatra.2020.10.020>



The final publication is available at

<https://doi.org/10.1016/j.isatra.2020.10.020>

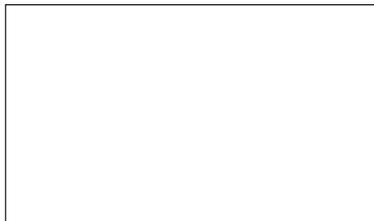
Copyright Elsevier

Additional Information

## Graphical Abstract

### **Detection and quantification of bar breakage harmonics evolutions in inverter-fed motors through the dragon transform**

V. Fernandez-Cavero, J. Pons-Llinares, O. Duque-Perez, D. Morinigo-Sotelo



## Highlights

### **Detection and quantification of bar breakage harmonics evolutions in inverter-fed motors through the dragon transform**

V. Fernandez-Cavero, J. Pons-Llinares, O. Duque-Perez, D. Morinigo-Sotelo

- Inverter-fed motors diagnosis through the analysis of the startups with optimized atom-based t-f transforms present in the technical literature
- Dragon atoms defined and build with shapes perfectly adapted to the harmonics trajectories to be detected, no matter how complex they are.
- Quantification and diagnosis performed obtaining the time evolutions of fault related harmonics amplitudes.

# Detection and quantification of bar breakage harmonics evolutions in inverter-fed motors through the dragon transform

V. Fernandez-Cavero<sup>a</sup>, J. Pons-Llinares<sup>b,\*</sup>, O. Duque-Perez<sup>c</sup> and D. Morinigo-Sotelo<sup>c</sup>

<sup>a</sup>Universidad Europea Miguel de Cervantes, Calle del Padre Julio Chevalier 2, 47012 Valladolid, Spain

<sup>b</sup>Instituto de Tecnologia Energetica, Universidad Politecnica de Valencia, Camino de Vera, s/n, 46022 Valencia, Spain

<sup>c</sup>GIR ADIRE, ITAP, Universidad de Valladolid, Paseo del Cauce 59, 47011 Valladolid, Spain

---

## ARTICLE INFO

### Keywords:

time-frequency analysis  
transient analysis  
fault diagnosis  
broken rotor bar  
induction motors  
inverter

## ABSTRACT

The problem of detecting and quantifying bar breakage harmonics in inverter-fed induction motors has not been solved by the time-frequency transforms present in the technical literature. The paper proposes a new transform, called dragon transform, to solve this problem. The dragon atoms are defined with shapes perfectly adapted to the harmonic trajectories in the time-frequency plane, no matter how complex they are, enabling the precise tracing of the harmonics to be detected. A quantification method is also proposed, which obtains for the first time in the technical literature, the time evolutions of the harmonic amplitudes during a complex transient such as the start-up and the steady state of an inverter-fed motor. The transform performance is validated testing the induction motor under different load levels.

---

## 1. Introduction

The majority of induction motors nowadays are inverter-fed. First, in fixed speed drives, the inverter allows adapting the speed to the load requirements, reducing the power consumption [1]: 25% reduction when running at half speed [2]. Second, the inverter is mandatory in variable speed drives. Among other drawbacks, line motor supply increases highly the stress during startups, causing faults as bar breakages. Nevertheless, even if startup currents are lower (they may reach twice the rated current), these stresses also appear in inverter-fed motors, especially when they work under overloads, and must perform regenerative braking, as in the case of cement or paper and pulp industries, or when the duty cycle contains frequent starts [3] and multiple steady-state speeds, as in electric traction.

Furthermore, the inverter higher harmonic content at low frequencies increases the temperature [4] and creates harmonic torques [5], enabling cage vibration resonances [6] (mechanical resonance cage fatigue failures cover 10% of total failures [7]), and finally increasing the rotor solicitations. Especially in electric traction with high power inverters with lower switching frequencies, covering wide speed ranges, and dealing with regenerative braking through bidirectional converters, the manufacturers are introducing design-based solutions to prevent bar breakages, as inclining two out of three bars in the junction with the short-circuit ring to hinder its detachment [8].

Therefore, rotor problems arise in inverter-fed motors, which can lead to winding damage [9], especially under centrifugal forces at high speeds [6], when the bars are detached from the slots [10], or the whole short-circuit ring is detached, as in the inverter-fed induction motor shown in [8]. Moreover, while the design and manufacture of other parts of the machine have improved, the rotor has not changed, and its percentage of the whole induction motor faults has increased [11]. Certain manufacturers have come up with possible solutions to this type of problem: improving torsional stiffness [12], replacing short-circuit rings by flexible wires in the slots [13], or using elements between bars to increase the stiffness and reduce the stress between the bar and the short-circuit rings [5].

Research has been focusing its efforts on developing methods of induction motor diagnosis based on current analysis, due to its advantages [8], even if vibration methods are more commonly used in industry [14]. Since inverter-fed motors work under changing speeds, the frequencies in the current change over time, and time-frequency transforms must be used to perform the analysis [15, 16]. Moreover, even under a long steady-state capture, the harmonics are more easily confused in its spectrum than in a time-frequency map related to a transient, taking into account that the harmonic content and noise caused by the inverter may overlap or hide the faulty harmonics, whose amplitudes also

---

 jpons@die.upv.es (J. Pons-Llinares)

ORCID(s): 0000-0002-3957-5042 (V. Fernandez-Cavero); 0000-0003-3756-1242 (J. Pons-Llinares); 0000-0003-2994-2520 (O. Duque-Perez); 0000-0001-6153-9438 (D. Morinigo-Sotelo)

depend on the Fundamental Component (FC) frequency and the control [17, 18, 19]. Unlike line-fed motors, the FC frequency changes when the motor is fed by an inverter [20]. Moreover, the slip frequency remains low, making the Bar Breakage Harmonics (BBH) evolve parallel and very close to the FC in the time-frequency plane [21, 22]. These two aspects make fault detection a challenge, whose solution is the purpose of this paper.

There are mainly two types of transforms that can be used to obtain the time-frequency trajectories of the components present in a signal: the Wigner-Ville Distributions (WVD) and the atom-based transforms. Regarding the WVD, they are not useful to obtain the evolutions of BBH in inverter-fed induction motors: the cross-terms introduced by this technique cannot be erased using a kernel when the evolutions of the components to be detected are too close to each other [23]. The Short Time Fourier Transform (STFT), which is the simplest atom-based time-frequency transform, is not able to trace separately the evolutions of the FC and the BBH: the FC energy disperses and hides the faulty harmonics evolutions [23]. The wavelet transform, which has been used in several works to diagnose inverter-fed induction motors [22, 20, 24, 25], does not improve the STFT result regarding bar breakages since the atoms used by this transform are adapted only for increasing frequencies following approximately a parabola. More advanced atom-based transforms, as the Adaptive Slope Transform (AST) [26], have been applied to detect eccentricities in inverter-fed induction motors [27], but as will be shown through the paper, they only achieve to obtain the evolutions during the steady-state when dealing with bar breakages under this type of supply. Finally, the last atom-based transform, the Chirplet Transform (CT) [8, 28], only achieves to distinguish the BBH trajectories during a certain part of an inverter-fed startup. Among other transforms, the Hilbert Huang Transform has been also applied to diagnose inverter-fed motors, but it cannot separate the faulty harmonics from the FC [23]. Finally, other transforms propose a non-uniform resampling [29] that facilitates the observation of the BBH when plotted in a space-frequency map instead of a time-frequency map. Nevertheless, they do not allow quantification, making the diagnosis impossible.

Concluding, the time-frequency transforms present in the technical literature do not achieve to obtain the evolutions of the BBH during the startup of an inverter-fed motor and the quantification of their energies to perform a diagnosis. Two approaches permit a quantification, but they only obtain a part of the trajectory (AST and CT), while a third approach enables plotting the evolution in a space-frequency map, without possible quantification. This is the first paper in which the trajectories of the BBH, during an inverter-fed induction motor startup and steady-state, are plotted with precision in the time-frequency plane as very thin lines, enabling the quantification of their instantaneous amplitudes.

The structure of the paper is as follows: Section 2 shows the time-frequency evolution of the faulty current components to be detected, pointing out the characteristics of the problem we are facing; Section 3 analyses the classic time-frequency atoms showing how their resolution trade-off hinders the detection of the faulty harmonics; Section 4 introduces the proposed Dragon Transform (DT), which enables precisely tracing the evolution of these harmonics, including a method for their amplitude quantification, and comparing its results to previous transforms; the experimental results are shown in Section 5, comparing healthy and faulty cases at different loads, and the conclusions are finally presented in Section 6.

## 2. Time-frequency evolutions of the harmonics to be detected

The fault diagnosis of an induction motor through its current analysis is as follows: the current of an ideally healthy motor only has healthy harmonics; each fault generates in the motor's current specific harmonics related only to that fault; the amplitude of the fault harmonics increases with the severity of the fault; a transform enabling the detection and quantification of the fault harmonics enables a diagnosis procedure. The objective of the analysis of a stator current signal with a time-frequency transform is to obtain the evolutions of the current signal components in the time-frequency plane (also called harmonics, even if some authors reserve this term only for steady state). If the fault components are present in the signal, their trajectories will appear in the transform result, enabling to detect them and quantify their amplitudes, and allowing to perform a diagnosis. Therefore, the evolution has to be traced completely and with enough precision to define a reliable quantification method of the harmonics amplitude.

To study which type of transform has to be applied to obtain such a result, the first step is the analysis of the "structure" of the stator current signal; i.e., which are the kind of evolutions that the transform applied has to be able to reflect in the time-frequency graph obtained. Let us analyse it through an example: the stator current of an inverter-fed induction motor with a broken rotor bar has been captured during a startup and the subsequent steady state (Fig. 1). The motor and inverter characteristics can be found in Section 5.

The frequencies of the fault harmonics to be detected depend on three key magnitudes of the motor: fundamental component frequency, slip and slip frequency. Let us give their definitions for a reader non expert in electric motors,

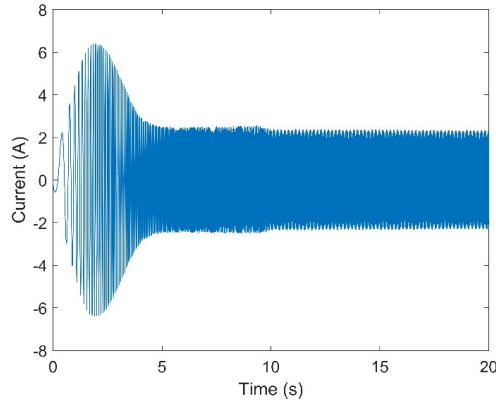


**Figure 1:** Stator electric current of an inverter-fed induction motor during a starting period of 10 seconds and a final steady-state operation.

and then analyse their time evolutions in an inverter-fed motor startup, to finally understand the shape of the BBH evolutions.

The output voltage generated by the inverter using a PWM scheme is rich in harmonic and interharmonic content. The harmonic with the largest amplitude is called the Fundamental Component (FC), and its frequency is  $f_{FC}$ . The FC fixes the speed of the rotating magnetic field, known as the synchronous speed  $n_s = 60f_{FC}/p$ , where  $p$  is the number of pole pairs of the motor. The motor slip is a dimensionless measure of the difference between the synchronous speed  $n_s$  and the mechanical rotor speed  $n$ :  $s = (n_s - n) / n_s$ . Finally, it can be demonstrated that the slip frequency,  $sf_{FC}$ , is the frequency of the rotor currents, measures the difference in Hz between the electric rotational frequencies of the magnetic field and the rotor, but more important in the context of this paper, it determines the distance between the frequencies of the FC and the BBH, as follows.

The frequencies of the BBH,  $f_{BBH}$ , are deduced in [30], and can be expressed in terms of the FC frequency  $f_{FC}$  and the slip frequency  $sf_{FC}$ :

$$f_{BBH} = (1 \pm 2s) f_{FC} = f_{FC} \pm 2(sf_{FC}) \quad (1)$$

Let us analyse how the time-frequency evolutions of these harmonics are obtained. First, the time evolution of the FC frequency can be obtained through the current captured using the method presented in [27] (therefore, the  $n_s = 60f_{FC}/p$  evolution is obtained too). The motor speed is acquired using a sensorless speed method [31], or directly using a sensor (if any installed), as in this paper. Then, the slip is obtained through the motor speed  $n$  and the synchronous speed  $n_s$ :  $s = (n_s - n) / n_s$ . The slip frequency is calculated multiplying  $s$  and  $f_{FC}$ . Finally, the time evolutions of the BBH are obtained applying (1).

The FC frequency, the slip, the slip frequency and the BBH trajectories in the time-frequency plane are shown in Fig. 2 for the case of the induction motor with a bar breakage whose startup current is shown in Fig. 1. The time evolutions shapes of the FC and slip frequency are generated by the motor control: the key point is to understand how these shapes influence the time evolutions of the BBH (the reason why the control creates these shapes is beyond the context of this paper).

During a startup of an inverter-fed induction motor, the motor control increases  $f_{FC}$  with time. For instance, Fig. 2a shows the FC time-frequency evolution for the current shown in Fig. 1. In this case,  $f_{FC}$  increases linearly with time from 0 Hz to 50 Hz, which is the frequency of the motor after the starting transient. The duration of the starting and the final value of the FC are fixed by the user, which in this case are 10 s and 50 Hz respectively (the user can fix the speed needed by the driven load, and then the control fixes the FC). The role of the inverter is to maintain the slip frequency low and approximately constant (between 1 and 2 Hz in this case, as observed in Fig. 2c). Therefore, if  $sf_{FC}$  is constant, and  $f_{FC}$  increases linearly with time,  $s$  describes the inverse evolution (Fig. 2b).

Finally, as stated in (1), the BBH frequencies are equal to the FC frequency, plus or minus twice the slip frequency, which is almost constant (1.5 Hz approximately). Then, if  $f_{FC}$  increases but the slip frequency remains approximately constant, as during an inverter-fed startup, according to (1), the frequencies of the BBH evolve parallel to the FC,

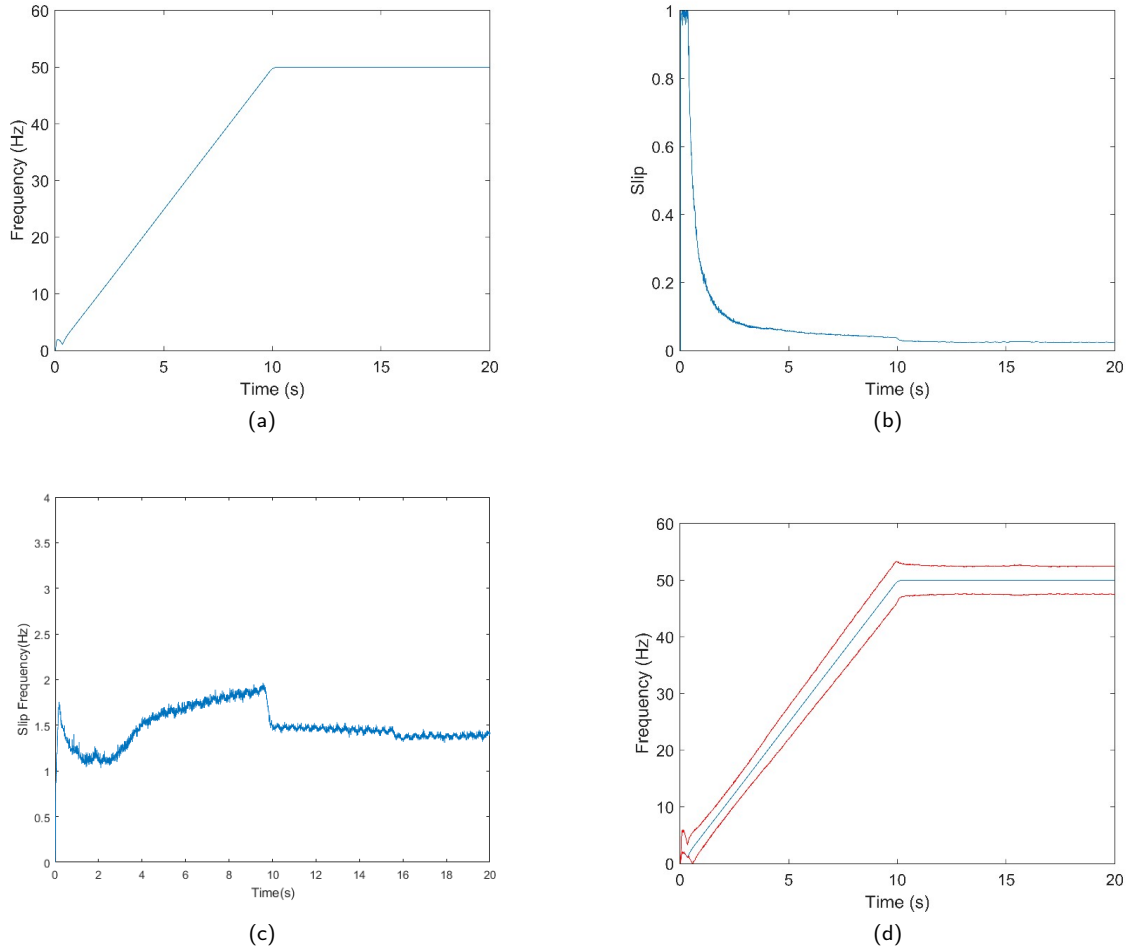


**Figure 2:** Time evolution of the following magnitudes, during the startup and subsequent steady state of the induction motor with a bar breakage (1): Fundamental Component (a), motor slip (b), slip frequency (c) and FC in blue together with bar breakage components  $f_{BBH}$  in red (d).

separated twice the slip frequency (3 Hz), towards higher or lower frequencies, depending on the sign used in (1). This is exactly what can be observed in Fig.2d, where the FC frequency has been plotted (blue) together with the BBH evolutions (red).

It can be concluded that, in the case of an inverter-fed motor, the BBH evolve very close to the FC. Taking into account that the FC has a much higher energy than the faulty harmonics, the detection of these harmonics is very difficult. The challenge is to represent the FC evolution in the time-frequency plane as a very thin line: if its energy spreads around its actual trajectory, being represented as a too thick line, the fault-related harmonic evolutions will be hidden.

### 3. Time-frequency atoms and resolution trade-off

Time-frequency transforms try to obtain the time-frequency evolutions of the components in an analysed signal. Basically, there are two types of transforms: the Wigner-Ville distributions and the atom-based transforms. The Wigner-Ville distributions are not considered here, since they introduce cross-terms, which are very difficult to remove using kernels when the harmonics are so close to each other as in this case (see previous section). On the other hand, atom-based transforms generate clearer results without cross terms. Nevertheless, they have an inherent resolution trade-off which has to be solved.

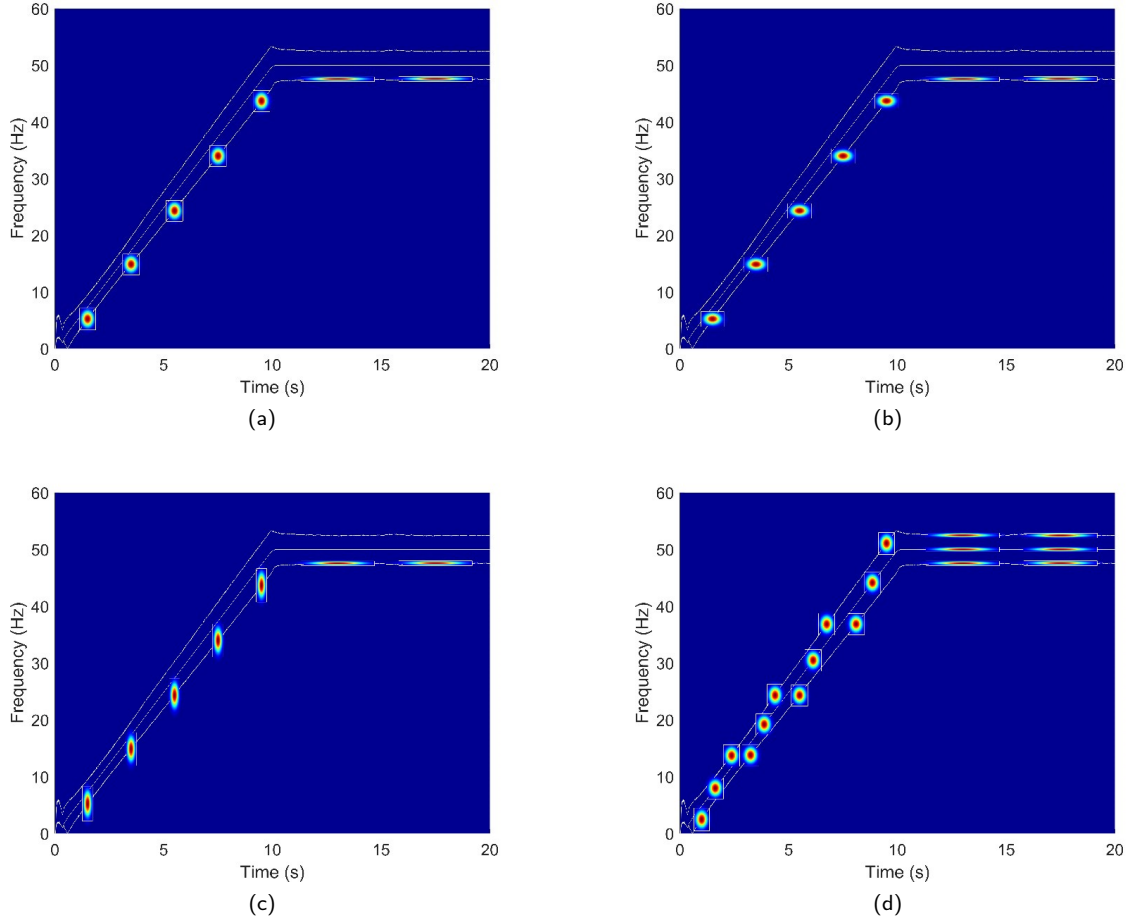


**Figure 3:** Time-frequency evolutions of the FC and the bar breakage related harmonics (white) together with the energy distribution of several time-frequency atoms along the lower sideband harmonic evolution, following the slope criterion (a), with a lower slope (b) with a higher slope (c) and distributed along the three evolutions, according with the slope criterion (d).

Briefly, a time-frequency atom is a function whose energy is well concentrated around a point of the time-frequency plane. Fig. 3a shows the same evolutions of the FC and the BBH of Fig. 2d, plotted in white. The time-frequency energy distribution of seven atoms has been represented too. These atoms are centred at different points along the Lower Sideband Harmonic path (LSH, bar breakage related harmonic below the FC). The present paper uses Gabor atoms  $\phi$ , defined by a Gaussian window  $g$ , with a time dispersion characterised by its deviation parameter  $\sigma$ , centred in  $t_c$ , normalised with a constant  $C_\sigma = 1/(\sqrt[4]{\pi}\sqrt{\sigma})$ , and modulated at a frequency  $f_c$ :

$$g(t) = C_\sigma e^{-\frac{(t-t_c)^2}{2\sigma^2}} \longrightarrow \phi(t) = g(t)e^{i2\pi f_c(t-t_c)} \quad (2)$$

The energy of each atom is confined in its respective enlarged Heisenberg box. This box, plotted in white in Fig. 3, describes how the energy of the atom disperses from its centre along the plane (see section 2 in [26] for a deep introduction). For instance, the five atoms centred along the startup have a box more or less squared, while the two atoms centred in points of the steady state have a flatter rectangular box, which describes the rectangular shape of their energy dispersion in the plane. The correlation between the atom and the signal to be analysed measures the energy of the signal inside the enlarged Heisenberg box of the atom; correlating is like multiplying the time-frequency energy distributions of the atom and the signal analysed. Everything outside the enlarged Heisenberg box of the atom is cancelled, and only the energy of the signal inside the box is measured. More precisely, it can be demonstrated that the

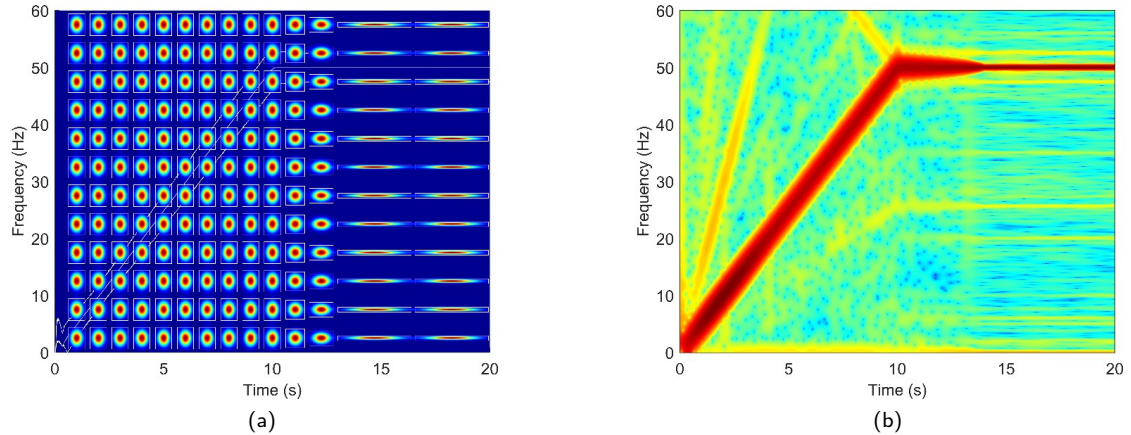


**Figure 4:** Time-frequency evolutions of the FC and the BBH (white) together with the family of time-frequency atoms fixed with the slope criterion (a) and the resulting analysis (b) of the current from the bar breakage motor (AST).

square of the correlation is a measure of the energy density of the signal inside the box. If the operation is repeated in several points of the time-frequency plane, correlating with atoms centred in those points, the energy density along the plane will be obtained, showing how the energy of the signal is distributed in time and frequency. The energy density of the signal will be high in the points of the time-frequency plane nearby harmonic trajectories, and low everywhere else. Therefore, the representation of the energy density of the signal obtained through atoms correlations gives the time-frequency evolutions of the harmonics contained in the signal analysed.

The question is: which is the best “shape” of the atom to be used? When atoms with “rectangular” energy distributions are used (as the ones shown in Fig. 3), the best shape is obtained applying the slope criterion [26, 27]: if an atom is centred in a certain point of a harmonic trajectory, the diagonal of its Heisenberg box must match the tangent to the harmonic trajectory at that point to capture the energy of that harmonic at that point. Since the LSH evolution along the motor startup is approximately rectilinear, the tangent at every of these points is the LSH trajectory itself. Therefore, the atoms used along the startup in Fig. 3a have a Heisenberg box diagonal that matches the evolution of the LSH. The atoms in the steady state, since the tangent to the LSH evolution is a horizontal line, should be completely flat. Nevertheless, this is not recommended since the atom energy would disperse in time from minus to plus infinity.

The problem of this approach is that the FC evolution crosses every of the five boxes of the atoms centred along the LSH trajectory during the startup. Therefore, when correlating those atoms with the signal analysed, even if they try to measure only the LSH energy around the points where they are centred, the FC energy would be measured too, since the correlation measures the energy inside the box, and those boxes contain parts of the FC evolution. If a flatter box is used (Fig.3b), we are trying to avoid crossing the FC evolution in the upper part of the box, but a bigger part is captured at the left part of the box. Analogously, if a taller box is used (Fig. 3c), the FC interacts less with the left part of the box, but crosses more in its upper part. The slope criterion has the best compromise, not only to capture the highest amount of the LSH energy [26], but also to avoid the FC.

Nevertheless, this is not enough. Fig.3d shows a family of atoms centred along the trajectories of three signal components using the slope criterion. It can be observed that, since the three evolutions are nearly parallel along the startup, the tangents to them are also parallel. Moreover, since the trajectories are almost linear, their tangents hardly change during the startup. Therefore, all the atoms along the startup, with diagonals matching the tangents, have nearly the same shape. Hence, to construct the final family of atoms to correlate with the signal, atoms with the same shapes are used along all the plane during the startup, changing to a flatter rectangular shape when the steady state arrives (Fig. 4a). The result of the transform, called Adaptive Slope Transform (AST, used in [26] to detect bar breakages in directly-fed motors, and in [27] to detect eccentricities in inverter-fed motors), is shown in Fig. 4b. As predicted, the atoms centred at the LSH evolution capture the FC energy, which reaches those points, hiding the LSH trajectory. In other words, the energy of the FC spreads around its evolution, hiding the trajectories of the bar breakage related components during the startup. Only during the steady state, an atom centred at the FC captures the FC energy, while

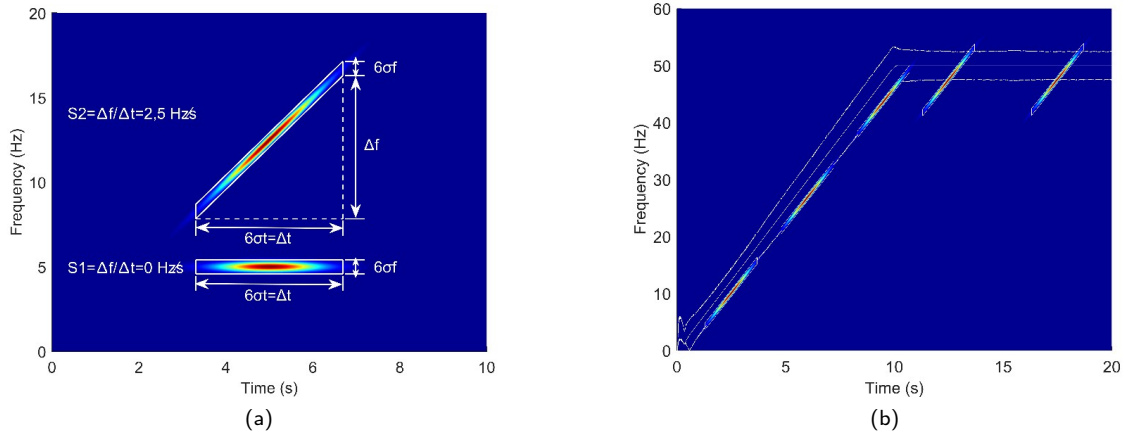


**Figure 5:** Constructing a chirplet type atom: energy distribution of chirplet atoms with 0 and 2.5 Hz/s slopes (left). Time-frequency evolutions of the FC and the bar breakage related harmonics (white) together with the energy distribution of several chirplet type atoms along the lower sideband harmonic evolution, adapted to that harmonic slope during the startup (right).

an atom centred in the LSH captures only its own energy. This is because the shape of the atoms are perfectly adapted to the harmonic evolutions that they are trying to detect, which appear traced as thin lines, enabling to distinguish the three harmonics.

The atoms can change their shapes from the classic rectangular dispersion of their energy. In a rectangular atom, as shown in (2), the window is modulated by multiplying with a complex exponential of angle  $\theta(t) = f_c(t - t_c)$  (expressed in degrees instead of radians). The derivative of that angle gives the frequency at which the window is modulated, which in this case it is constant:

$$\theta(t) = f_c(t - t_c) \longrightarrow \frac{d\theta(t)}{dt} = f_c \quad (3)$$

Let us construct an atom with a flat rectangular dispersion of its energy (lower atom in Fig. 5a). This is achieved by taking a high deviation parameter  $\sigma$  in (2): the energy of the atom disperses in time. Then, to construct the upper atom in Fig. 5a, instead of modulating the Gaussian window at a constant frequency  $f_c$  (as in (2)), the modulation is performed as follows:

$$g(t) = C_\sigma e^{-\frac{(t-t_c)^2}{2\sigma^2}} \longrightarrow \phi(t) = g(t)e^{i2\pi(f_c(t-t_c) + \frac{S}{2}(t-t_c)^2)} \quad (4)$$

The instantaneous frequency in (5) increases linearly in time with a slope  $S$ , being  $f_c$  when  $t = t_c$ :

$$\theta(t) = f_c(t - t_c) + \frac{S}{2}(t - t_c)^2 \longrightarrow \frac{d\theta(t)}{dt} = f_c + S(t - t_c) \quad (5)$$

The slope  $S$  determines the ‘‘inclination’’ of the atom. If  $S = 0$  Hz/s, then equations (2) and (6) are equal, and taking  $f_c = 5$  Hz, the lower atom in Fig. 5a is obtained, which has no inclination. If  $S = 2.5$  Hz/s, and taking  $f_c = 12.5$  Hz, the upper atom is constructed: it has an energy dispersion that follows a straight line; the slope  $S$  coincides with the inclination of the line that the energy dispersion is going to follow, while its main centre frequency is still  $f_c$ . These atoms are called chirplets. The resulting transform is called Chirplet Transform (CT). In Fig. 5b the same evolutions of the FC and the bar breakage related harmonics of Fig. 2d are plotted in white. Moreover, the energy distributions of five chirplet atoms have been represented. The chirplets have been chosen with a slope  $S = 5$  Hz/s, equal to the slope of the LSH evolution during the startup (evolves from 0 to 50 Hz in 10 s). This way, their shape fits the evolution of the harmonic to be detected during the startup. They have been centred in three points of the startup and two points of the steady state. Since the FC and the other bar breakage related harmonics evolve in parallel, the chirplets constructed with this slope would also capture their evolutions during the startup.

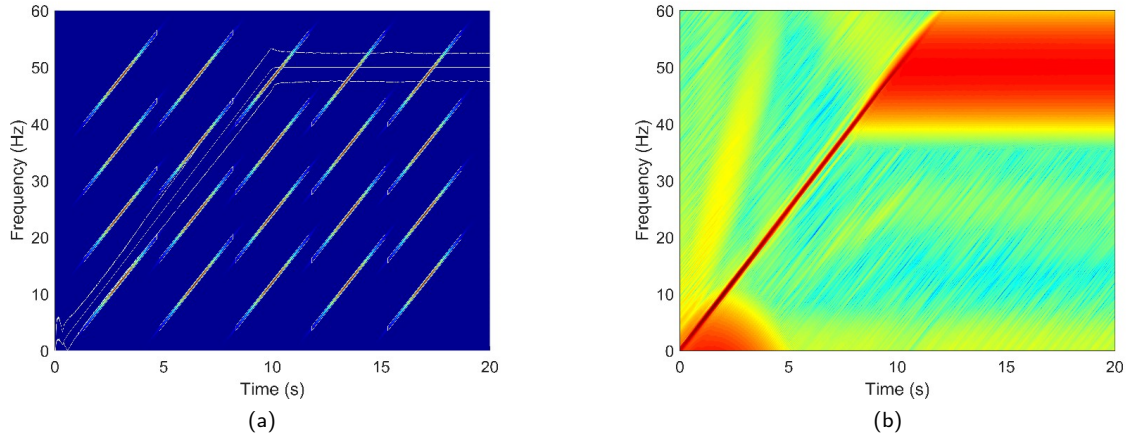


**Figure 6:** Time-frequency evolutions of the FC and the bar breakage related harmonics (white) together with the family of chirplet atoms adapted to the FC slope during the startup (left) and the resulting analysis (right) of the stator current of a motor with a broken rotor bar.

Figure 6 shows a whole family of chirplets distributed along the time-frequency plane, together with the evolutions of the FC and the BBH to be detected. One of the drawbacks of the CT is that the inclination of the chirplets must be the same for every point of the plane analysed. The chirplets are chosen with a 5 Hz/s slope, adequate to match the evolutions of the three harmonics during the startup. The result of the CT is shown in Fig. 6b. It can be observed that the FC evolution appears as a very thin line during a certain part of the startup. Same thing happens with the bar breakage components. In this region, their evolutions can be distinguished very well. Nevertheless, a chirplet centred with this shape around a point of the FC steady state captures its energy, unless it is centred far away from its evolution. Therefore, the FC energy spreads widely around its evolution, masking the end of the startup, and everything around the steady state, and particularly hiding the evolutions of the BBH.

In this section, the best results have been obtained with the rectangular shaped atoms (AST), and with the inclined linear shaped atoms (CT). As seen through the presented results, these time-frequency transforms do not achieve to obtain the evolutions of the BBH during the startup of an inverter-fed motor. This is due to the fact that, in this case, the faulty harmonics evolutions are too close to the FC trajectory. To prevent the FC from hiding the faulty harmonics, its evolution has to be plotted as a thin line. Nevertheless, this only happens during the steady state for the AST, and during a part of the startup for the CT. Therefore, the AST only achieves to detect the BBH evolutions during the steady state, and the CT only during a section of the startup. None of them allow to trace the whole evolution of the faulty harmonics. For this reason, a new transform is defined in the following section, based on a new type of atom.

## 4. The Dragon Transform

As seen in the previous sections, the main problem to detect the FC and the bar breakage evolutions in an inverter-fed induction motor startup is that they are too close to each other. The transform must be able to trace them as very thin lines to distinguish them in the time-frequency plane. This is achieved when the energy dispersion of the used atoms follows the evolution of the component to be detected. Then, the energy dispersion of the component itself, when represented in the time-frequency map, takes place also along its own evolution. As a result, the component evolution is traced as a very thin line, without nearly any thickness. In the present section, the dragon atoms (which have the mentioned characteristics) are defined and built. Then, the Dragon Transform (DT), based on the use of the dragon atoms, is also defined and applied. Finally, a quantification method is introduced to obtain the instantaneous amplitudes of the harmonics detected.

### 4.1. Building atoms following arbitrary evolutions

The dragon atoms are defined as atoms whose energy disperses following the trajectory of the component to be detected. In other words, the shape of the atom fits the evolution of the harmonic component. The modulation must

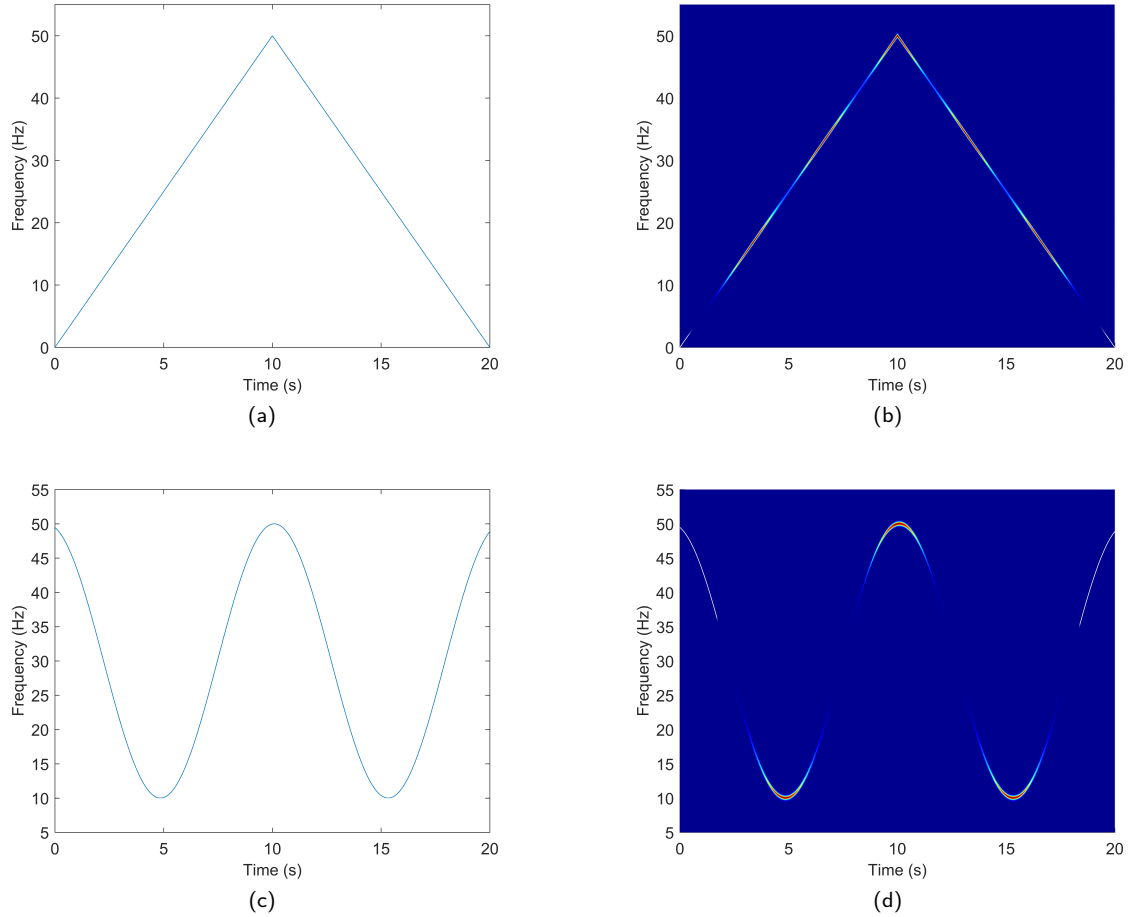


**Figure 7:** Time-frequency evolutions of mono-component synthetic signals ((a) and (c)), energy distribution of dragon atoms following these evolutions ((b) and (d)), for a triangular evolution and for sinusoidal frequencies pulsating around 30 Hz.

be performed differently at each time instant to achieve this. More precisely, the window must be modulated using an angle  $\theta(t)$  in the complex exponential, whose time derivative is equal to the time evolution of the frequency of the component  $f(t)$ :

$$g(t) = C_{\sigma} e^{-\frac{(t-t_c)^2}{2\sigma^2}} \longrightarrow \phi(t) = g(t) e^{i2\pi\theta(t)} \longrightarrow \frac{d\theta(t)}{dt} = f(t) \quad (6)$$

Figure 7 shows the time evolutions of the frequencies from two mono-component synthetic signals. The first monocomponent signal has first a linearly increasing frequency and then changing to a linearly decreasing frequency (Fig. 7a), while the second describes a frequency changing sinusoidally in time (Fig. 7c). The figure also shows (Fig. 7b and Fig. 7d), the energy distributions of five dragon atoms for each case, centred in different points and defined to fit the trajectories of the mono-component signals. As it can be observed, the dragon atoms follow precisely the time-frequency evolutions of the synthetic signal mono-components, not only during their rectilinear periods, but also during the points of change.

The dragon atoms, which have been defined and built in the present section of the paper, can adapt to the shape of any harmonic time evolution, no matter how oddly its frequency changes in time. Their shape is elongated and adaptable, like that of a snake or an Asian dragon (in Asian literature, dragons are shaped like snakes), and that is why we have called them dragon atoms. As it will be shown in the next subsection, this will permit to plot a harmonic

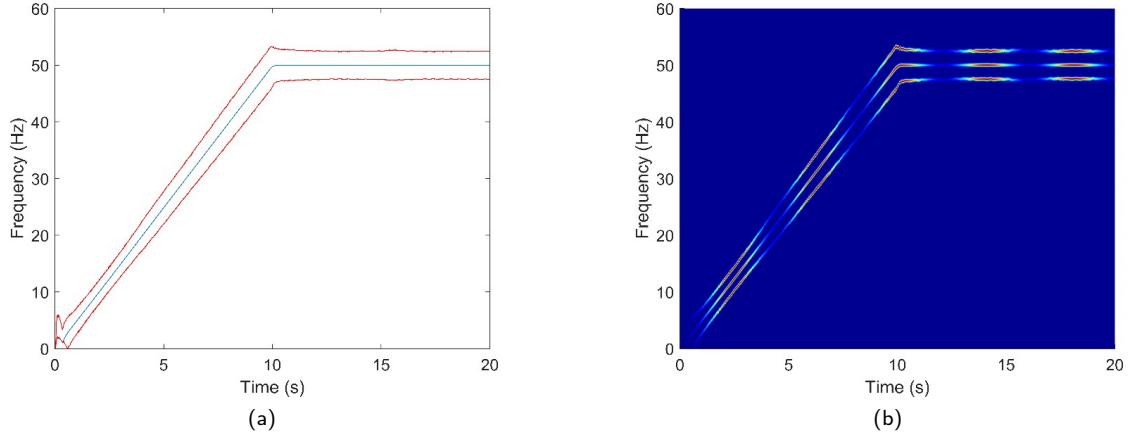


**Figure 8:** (a) Time-frequency evolutions of the FC (blue) and the broken bar related harmonics (red). (b) Energy distributions of several dragon atoms along the three trajectories.

evolution as a very thin line, because when a dragon atom is used, the energy dispersion happens along the harmonic evolution itself.

## 4.2. Transform definition

The Dragon Transform (DT) is defined as the correlation between the signal to be analyzed,  $h$ , with a family of dragon atoms,  $\phi$ :

$$\langle h, \phi \rangle = \int_{-\infty}^{+\infty} h(t)\phi^*(t)dt = \int_{-\infty}^{+\infty} h(t)C_{\sigma}e^{-\frac{(t-t_c)^2}{2\sigma^2}}e^{-i2\pi\theta(t)}dt \longrightarrow \frac{d\theta(t)}{dt} = f(t) \quad (7)$$

The correct definition of the family of dragon atoms is the key point. To start with,  $t_c$  is the time instant where the atom is centred (fixed when the time instant analysed by the atom is chosen). As previously mentioned in the explanation of Fig. 5a, the deviation parameter is taken high enough to obtain a thin atom; the constant that normalises is automatically defined  $C_{\sigma} = 1 / \left( \sqrt[4]{\pi} \sqrt{\sigma} \right)$ . The angle in the complex exponential of equation (7) is the most important remaining parameter.

Basically, two possible situations must be considered: an atom centered in a point where a component of the signal crosses, and an atom centered in a point where no component of the signal crosses. In the case of the signal analyzed (the startup current of an inverter-fed induction motor), there are three components whose evolutions must be properly traced to diagnose the rotor condition: the FC and the rotor broken bar related harmonics (plotted in blue and red respectively in Fig. 8a). For this first case, in which the atom is centered in one of these three trajectories, the atom must simply fit the evolution to be detected. To achieve this, the time evolution of the frequency component must be obtained as follows, taking  $k = 0$  for the FC,  $k = 1$  for the Upper Sideband Harmonic (USH), and  $k = -1$  for the LSH:

$$\frac{d\theta(t)}{dt} = f(t) = |1 + 2ks(t)|f_{FC}(t) \quad (8)$$

Once the derivative of the angle is determined, numerical integration is applied (taking a zero initial value, since it has no effect on the result of the transform), and the resulting angle is used in (7) to obtain the correlation. Fig. 8b shows the energy distributions of fifteen dragon atoms, centered at several points of the FC, LSH and USH trajectories, defined following this procedure.

Let us approach the second situation: atoms centred in points where no harmonic evolution crosses. The procedure is to define an evolution crossing that point and parallel to the FC, LSH and USH evolutions, and then, define the atom to fit that evolution. Giving positive values to  $k \in \mathbb{Z}$ , (8) describes evolutions parallel to the USH evolution tending

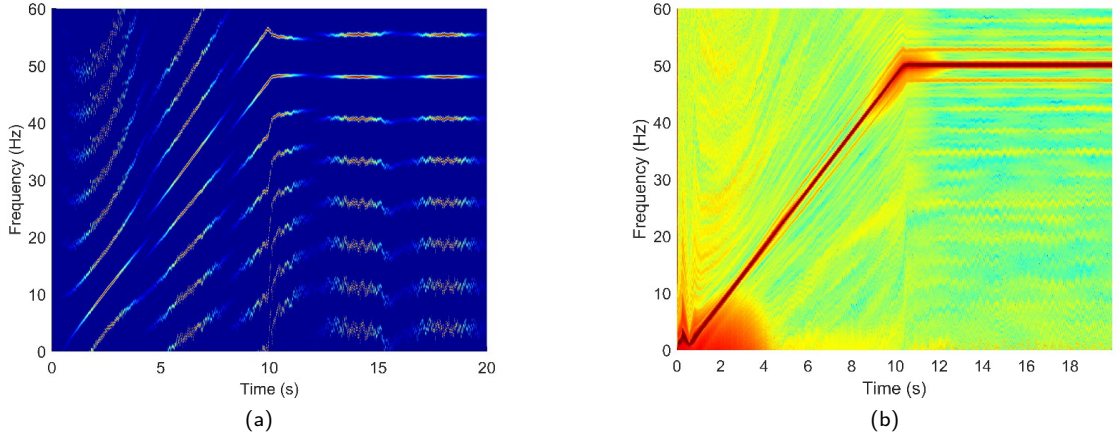


**Figure 9:** Family of dragon atoms (a) and the resulting analysis through Dragon Transform (b) of the stator current of a motor with a broken rotor bar.

to higher frequencies. On the contrary, if negative values are assigned to  $k \in \mathbb{Z}$ , the equation describes evolutions parallel to the LSH towards zero. Generally speaking, if instead of taking  $k \in \mathbb{Z}$ , we take  $k \in \mathbb{R}$ , a whole family of parallel trajectories are defined in the time-frequency plane (in which the FC, LSH and USH evolutions are included when  $k = 0$ ,  $k = -1$ , and  $k = 1$  are taken respectively). All these trajectories are parallel: they do not cross each other. Therefore, for each point of the time-frequency plane  $(t_c, f_c)$ , there exists only one harmonic evolution crossing that point. The value of  $k \in \mathbb{R}$ , which defines the evolution crossing  $(t_c, f_c)$ , is given by:

$$k(t_c, f_c) = \frac{1}{2s(t_c)} \left[ \frac{f_c}{f_{FC}(t_c) - 1} \right] \quad (9)$$

If an atom is centred in  $(t_c, f_c)$ , the value of  $k(t_c, f_c)$ , which defines the evolution crossing  $(t_c, f_c)$ , is obtained using (9). Then, the evolution itself is obtained using (8):  $f(t) = |1 + 2k(t_c, f_c)s(t)|f_{FC}(t)$ . Then, that frequency time evolution is numerically integrated to obtain the angle finally applied in (7). To conclude, the only difference between the procedure based on an atom that is centred in the FC, LSH or USH evolutions, and an atom centred anywhere else, is that for the first case  $k = 0$ ,  $k = -1$ , and  $k = 1$  are taken respectively, and for all the other cases  $k$  is calculated using (9). In fact, if a point of the plane contained in the evolutions of FC, LSH or USH is considered, and the value of  $k$  is calculated through (9), it will give as a result  $k = 0$ ,  $k = -1$ , and  $k = 1$ . Therefore, exactly the same procedure can be applied for every point of the time-frequency plane.

If this procedure is applied to the stator current analysed, the family of dragon atoms shown in Fig. 9 is constructed. It can be seen that the further we move from the FC evolution, a bigger “ripple” appears in the energy dispersion of the atoms. This is caused by an inherent ripple in the speed measured, which is transferred to the slip, and finally to the time-frequency evolutions obtained through (8), which have to be followed by the dragon atoms. Since in (8)  $k$  multiplies the slip, the ripple in the frequencies calculated through (8) will get higher for higher  $|k|$ , and  $|k|$  increases when moving far from the FC trajectory ( $k = 0$  along the FC evolution). As it can be seen in Fig. 9, the dragon atoms even achieve to follow those ripples of the time-frequency evolutions obtained through (8). The result from the correlation of the signal with the family of dragon atoms is shown in Fig. 9b. Several zooms of this result can be seen in Fig. 10.

As it has been shown through the results, the dragon atoms adapt perfectly to the evolutions of the FC (Fig. 8b) and the BBH, not only during the startup, but also during the steady state. Moreover, it has been constructed a smooth family of dragon atoms (Fig. 9a), whose shapes change uniformly from one to the next, following evolutions that do not cross. As a result, the trajectories of the FC, LSH and USH are represented very precisely in the time-frequency plane as perfectly traced thin lines (Fig. 9b). Even if their evolutions are very close, due to the lack of thickness when plotted in the time-frequency plane, they can be distinguished along the whole captured transient (startup and steady state). Particularly, in Fig. 10, the evolutions at the beginning, the middle and the end of the startup can be observed

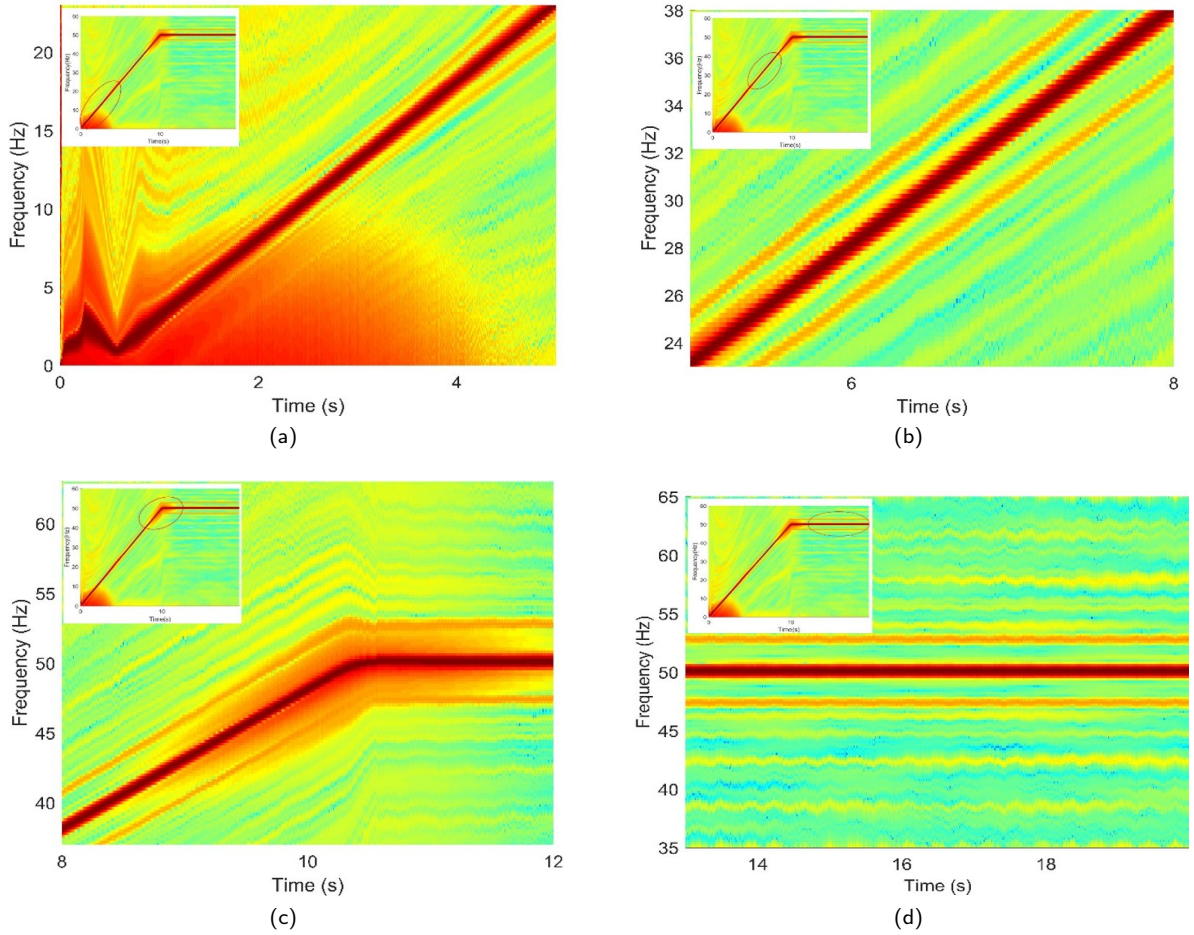


**Figure 10:** Several zooms of the Dragon Transform results shown in Fig. 9b.

separately, being able to follow their frequency change when the steady state arrives, and finally describing horizontal evolutions. To conclude, the Dragon Transform enables a very easy visual detection of the components evolutions when zooming, but it also enables to propose a quantification method to obtain its instantaneous amplitudes, and perform a reliable diagnosis, as shown in the next subsection.

### 4.3. Synthesis and comparison with previous transforms

In this section, the DT is directly compared to previous transforms, a brief physical interpretation of how the DT and its atoms work is given, its key advantages with respect to previous transforms are clarified and finally its calculation through an algorithm is synthesised.

The atom-based time-frequency transforms can be divided into three groups: transforms with rectangular atoms (like those used by the Short Time Fourier Transform, STFT, Wavelet Transform, WT, S transform, ST, and Adaptive Slope Transform, AST), transforms with chirplet atoms (whose energy dispersion follows a linear time-frequency evolution, as in the Chirplet Transform, CT) and dragon atoms (whose energy dispersion follows an arbitrary time-frequency evolution, as in the Dragon Transform (DT)).

As shown in [23], rectangular atoms are not able to obtain the evolutions of the BBH during startup of inverter-fed motors: no matter what is the shape of the atom centred in the BBH evolution, it will capture the energy of the FC (see Fig. 3), since the evolutions are too close. Therefore, the FC will cover the BBH evolutions. The AST obtains the best results: using a flat atom in steady state it captures the evolutions in that zone, but only the FC evolution is captured during the startup. The WT is also adaptable, but the shape of the atoms change only with frequency and in

a certain way that is only suited for parabolic evolutions. The ST results are not shown in [23], even so it has the same drawback as the WT: good frequency resolution and bad time resolution at low frequencies, bad frequency resolution and good time resolution at high frequencies (which is not suited for an arbitrary evolution of the harmonics).

Let us compare AST, CT and DT: Fig. 11 combines in one the previously shown figures of the atoms families and the results for these three transforms. For a better understanding, let us start by comparing the equations that define the atoms family for each transform. As stated before, all three transforms are defined as the correlation between the signal to be analysed  $h$  and a time-frequency atom  $\phi$  which in this paper is defined as a Gaussian window modulated with a complex exponential:

$$\langle h, \phi \rangle = \int_{-\infty}^{+\infty} h(t)\phi^*(t)dt \longrightarrow \phi(t) = C_{\sigma} e^{-\frac{(t-t_c)^2}{2\sigma^2}} e^{-i2\pi\theta(t)} \quad (10)$$

The first difference between the three transforms is the value of  $\sigma$  (higher  $\sigma$ , flatter atom). In the case of the AST,  $\sigma$  changes along the time-frequency plane, while in the CT and DT  $\sigma$  has a constant and high value. For instance, in Fig. 11a  $\sigma = 3.989$  for the atoms used during the steady state (big  $\sigma$ , big dispersion along time, flat atoms), while  $\sigma = 0.1784$  for the atoms used during the startup (good trade-off between dispersion in time and frequency: more squared atoms); the slope criterion [26] has been applied to assign values to  $\sigma$ . In the case of the CT and DT all the atoms have the same  $\sigma$ , which has a big value to start with flat atoms (as the AST steady state atoms). The atoms will finally be inclined (CT, Fig. 11c) or follow arbitrary evolutions (DT, Fig. 11e) when changing the angle of the complex exponential as follows.

The second difference between the transforms relies on how the angle of the complex exponential  $\theta(t)$  is defined. Let us recall that multiplying a window with a complex exponential  $e^{i2\pi f_c t}$  (usually called modulation), implies translating the window in frequency to  $f_c$  (also called frequency shifting). More generally, multiplying by  $e^{i2\pi\theta(t)}$  implies translating in frequency to  $d\theta(t)/dt$ . Therefore,  $d\theta(t)/dt$  indicates at which frequency the energy of the atom is centred, which might change in time; only if  $d\theta(t)/dt$  is constant (as with  $\theta(t) = f_c t$ ) the frequency shifting does not change with time, and the atom's energy is shifted to the same frequency for every time instant.

As observed in (11),  $d\theta(t)/dt$  is a constant for the AST, hence the frequency at which the atom is centred does not change with time, and all the AST atoms have a rectangular shape (Fig. 11a). This concept is better understood when analysing the CT. For the CT,  $d\theta(t)/dt$  changes linearly with time. Since with the CT a big  $\sigma$  is used, a flat atom like the one shown in the lower part of Fig. 5a is obtained. In this atom, for each time instant, the frequency at which the energy is centred is the same (like in the AST). When  $d\theta(t)/dt$  follows a linear evolution, the frequency at which the energy is centred changes linearly with time, obtaining an atom like the one shown in the upper part of Fig. 5a, or the family of atoms shown in Fig. 11c. Then, why to follow a straight line, if an arbitrary evolution can be chosen, in order for the atom to perfectly adapt to that evolution? To obtain this,  $d\theta(t)/dt$  must be equal to the instantaneous frequency to be followed: this is the case of the DT. If the FC and BBH evolutions must be followed (and parallel evolutions to those in the rest of the time-frequency plane, as explained in the previous subsection), the atom's family obtained are shown in Fig. 11e.

$$\left\{ \begin{array}{ll} \text{AST} & \frac{d\theta(t)}{dt} = f_c \quad \longrightarrow \quad \theta(t) = f_c(t - t_c) \\ \text{CT} & \frac{d\theta(t)}{dt} = f_c + S(t - t_c) \quad \longrightarrow \quad \theta(t) = f_c(t - t_c) + \frac{S}{2}(t - t_c)^2 \\ \text{DT} & \frac{d\theta(t)}{dt} = f(t) \text{ arbitrary} \quad \longrightarrow \quad \theta(t) = \int f(t)dt \end{array} \right. \quad (11)$$

The basic relationship between the atoms family used and the transform result obtained is: the harmonics time-frequency evolutions are obtained in a transform result as lines with a certain thickness dispersing around their real evolution the same way the energy of the atoms used disperses. For instance, since the atoms used by the AST during the startup (10 first seconds) are more or less squared (Fig. 11a), the energy of the FC disperses during the startup more or less the same way in time and in frequency, appearing as a thick line, instead of a perfectly thin line showing its real trajectory. When the steady state is reached, a flat atom dispersing mainly in time generates dispersion also mainly in that direction: since the FC and BBH evolutions are horizontal, their energy disperses along their own trajectory, and they appear as very thin lines, being able to distinguish them. The chirplet atoms used in Fig. 11a have an energy

dispersion parallel to the FC evolution during the startup. Therefore, the evolutions are traced in the transform result with a dispersion on that same direction. This is beneficial for the startup, since the FC dispersion takes place along its own evolution, being able to trace it as a very thin line and separately from the BBH. Nevertheless, dispersion in that direction applied to the steady state turns the FC steady state evolution into a very thick line. Since the dragon atoms follow perfectly the trajectories of the harmonics to be captured, the dispersion of these harmonics energy when traced in the transform result takes place in the direction of their own trajectories, not only during the steady state (like in the AST), or during the startup (like in the CT), but during all the transient, even when the harmonics change from a linear time evolution, to a horizontal line.

To better understand the type of result obtained for each atoms family, it must be recalled that when applying the correlation between the atom and the signal analysed, the result obtained is the energy of the signal in the zone of the time-frequency plane covered by the atom's energy. Since the atoms used by the AST in the steady state are very thin and horizontal, if they are centred at 50 Hz they capture the FC energy at that point, but if they are moved slightly to upper or lower frequencies, the zone where the atom's energy is confined will not include the FC evolution, and the result will be very low. In other words, the result is high only when the atoms are centred in the real FC evolution, and if they are slightly separated from that evolution, the energy captured decreases dramatically. Therefore, the energy will be big in a very thin line around the real FC evolution.

What the Dragon Transform achieves is to construct atoms that follow the evolutions of the harmonics to be detected: if they are centred in a point of the real harmonic evolution, they will produce a big energy result in the transform when correlating with the signal analysed, but a very low when slightly separated from that real trajectory. Therefore, the trajectories are traced as very thin lines, no matter how complex their evolution is.

This new transform can be used to track any harmonic trajectory in the time-frequency plane, healthy or faulty, because adaptability is one of its key features. Therefore, it can be used to detect other type of faults in induction motors, as mixed eccentricity. Nevertheless, even if only the dragon atoms have this characteristic, and can obtain the harmonics evolutions as perfectly thin lines, not all the problems (diagnosis or others), need to obtain the trajectories with that precision in order to be solved. For instance, detection of mixed eccentricity has been solved using the AST, even if the thickness with which the trajectories are traced in the transform result are quite big [27].

Finally, let us synthesise the DT calculation through an algorithm. Before applying the transform, the time evolutions of  $s$  and  $f_{FC}$  must be obtained:  $s(t)$  and  $f_{FC}(t)$ , as explained in Section 2. As stated before, first step is to assign a high enough value to  $\sigma$ , to obtain an atom flat enough:  $\sigma = 3.989$  implies that the atom's energy disperses in time over 3 s approximately (as observed in the atom centred at  $t_c = 14$  s and  $f_c = 48$  Hz in Fig. 11e), which is enough for a 20 s signal. With this  $\sigma$ , the atom slope (defined as the quotient between the dispersion in frequency and in time [26]) is  $P = 1/(2\pi\sigma^2) = 0.01$  Hz/s. When analysing longer signals, higher  $\sigma$  (lower  $P$ ), might be used. Once the flatness of the initial atom is fixed, the following procedure is repeated for each point  $(t_c, f_c)$  of the time-frequency plane:

$$\left\{ \begin{array}{l} (1) \text{ Choose a point of the time-frequency plane: } (t_c, f_c) \\ (2) \text{ Obtain } s \text{ and } f_{FC} \text{ at } t_c: s(t_c) \text{ and } f_{FC}(t_c) \\ (3) \text{ Calculate: } k(t_c, f_c) = \frac{1}{2s(t_c)} \left[ \frac{f_c}{f_{FC}(t_c)-1} \right] \\ (4) \text{ Obtain the time evolution of the frequency to be captured: } \frac{d\theta(t)}{dt} = |1 + 2k(t_c, f_c)s(t)| f_{FC}(t) \\ (5) \text{ Integrate in time the previous expression: } \theta(t) = \int |1 + 2k(t_c, f_c)s(t)| f_{FC}(t) dt \\ (6) \text{ Construct the atom: } \phi(t) = C_\sigma e^{-\frac{(t-t_c)^2}{2\sigma^2}} e^{-i2\pi\theta(t)} \\ (7) \text{ Correlate the atom and the signal: } \langle h, \phi \rangle = \int_{-\infty}^{+\infty} h(t)\phi^*(t) dt \end{array} \right. \quad (12)$$

Step (3) is specific of BBH detection (meaning of  $k(t_c, f_c)$ , has been deeply analysed in Section 4.2), while steps (4) and (5) have been written using the formula for the time evolution of BBH frequencies (first presented in Section 2). If another set of harmonics have to be detected, the time derivative of the atom angle  $d\theta(t)/dt$ , stated in step (4), must be equal to the time evolution of the new harmonics frequencies  $f(t)$ .

#### 4.4. Quantification method

The quantification method presented allows to obtain the time evolution of the harmonics amplitudes through the whole capture (the startup and its transition to the steady state). To achieve this goal, the Dragon Transform result is plotted in 3D, from two different perspectives (Fig. 12). In Fig. 13a, the same result as in Fig. 12a is represented, but including three arrows signalling the evolutions of the BBH: two for the LSH and one for the USH. Then, a frequency band is defined around the LSH evolution obtained through (8) (FC and speed evolutions captured as explained in Section 2). That frequency band is represented in blue in Fig. 13b. The width of the band is lower at the beginning of the startup and changes in the steady state part, where more precision is needed. For each time instant, all the transform results within the defined band are considered to find their maximum. That maximum is the energy of the LSH evolution, plotted in red (Fig 13b). The same procedure is applied to the USH, plotting the frequency band in green. The LSH and USH evolutions (red, Fig. 13b), are finally superimposed in blue to the 3D result shown in Fig. 14a. This enables to obtain, for each time instant, the instantaneous amplitude (in dB with respect to the FC amplitude), of the LSH and USH. These instantaneous amplitudes are finally plotted in Fig. 14b, in blue and green respectively.

To conclude, this is the first paper that shows the evolutions of the bar breakage components during a complex transient as the startup, and the following steady state, of an inverter-fed induction motor, and it also quantifies its amplitudes. Moreover, the evolutions are obtained completely, and with high precision, thanks to the Dragon Transform here defined.

### 5. Experimental results

Some experimental tests have been performed in a laboratory to prove the great capabilities of the Dragon tTransform. The induction motor tested has a 1.1 kW rated power, and 1410 rpm rated speed. The motor has been connected in star, being the rated line voltage and current 400 V and 2.6 A respectively. A hole has been drilled in the rotor cage to simulate a bar breakage. The frequency converter used to feed the motor is an Allen Bradley PowerFlex 40 inverter. This inverter has been programmed to startup the motor in 10 s, through a FC frequency increasing linearly in time, starting at 0 and reaching 50 Hz in steady state (as seen in blue, in Fig. 15, for the two load levels used (low at 15a and high at 15b). An electromagnetic powder brake by Lucas Nülle has been used as the motor load. A Hall effect sensor by LEM is used to collect the stator motor currents (at a sampling frequency of 5 kHz), connected to an acquisition board (cDAQ-9174, National Instruments), USB controlled through a PC.

Inverters offer different types of startups, but linear start-up is the most commonly used. In this starting, the FC frequency increases linearly over time until it reaches its final operating value. The inverter employed in this paper was programmed with this type of start-up and this explains the results displayed in Fig. 2. Inverters also have different control methods. Among the open-loop control alternatives, the constant  $V/f$  is the most common and the one used in the experimentation of this work.

The motor has been tested under two load levels and two condition states (healthy and with one broken rotor bar). At the first load level, the motor is at 51% of its rated load (2.6 Nm). The second level is achieved through a 3.8 Nm load torque (74% of the rated load). The methodology presented in the paper has been applied to both cases and two condition states, whose results are shown in Fig. 15 (motor with a broken rotor bar) and Fig. 16 (healthy motor): low load at the left, and high load at the right. The trajectories of the FC (blue) and the BBH (red) are shown at the top of both figures. The FC evolution has been obtained applying to the collected stator current the method presented in [27]. The control unit of the electromagnetic powder brake measures torque and speed, which is used to calculate the slip, necessary to plot the BBH trajectories. The DT has been applied to these four currents, as explained in previous sections. The results are displayed in Fig. 15c and 16c (for low load) and Fig. 15d and 16d (for high load). The fault quantification is the energy density along the trajectories of the BBH, which are shown at the bottom part of Fig. 15 for the faulty motor and the healthy motor in Fig. 16. In this last case, the energy during the start-up is around -130 dB (Fig. 16e and 16f). When the rotor has a broken bar, the energy of the fault-related harmonic increases to -100 dB (Fig. 15e and 15f), and this increment of the energy along the trajectory of the fault-related harmonic is the foundation of the motor diagnosis.

As shown in the present section, the DT works well in both low and high load conditions. The differences observed are only related to how close the fault-related harmonics evolutions are to the FC trajectory. The low load condition is most challenging since the evolutions are closer than the other case (this is why this case has been chosen to show how the DT works in previous sections). The quantification results obtained are very similar for both cases: the BBH amplitudes do not vary significantly with the load, for an induction motor started up through an inverter. It can be

concluded that the DT allows detecting the BBH, even when they evolve very close to the FC in low loaded motors, precisely showing its evolution along the inverter-fed start-up, and obtaining the energy density time evolution of the faulty harmonics to quantify the rotor fault.

## 6. Conclusions

As introduced in the abstract, and further explained through the paper, the high harmonic content in the stator currents introduced by inverters stimulates bar breakages in induction motors, due to the temperature increases, harmonic torques generated, the increased chances of mechanical resonances and the final increment in rotor solicitations, especially in applications with overloads, regenerative braking or with frequent startups and change of steady state speeds. Nevertheless, the detection of the broken rotor bars components evolutions is very difficult due to its vicinity to the FC. This paper presents an optimization of atom-based transforms present in the technical literature: the FC evolution is only traced as a thin line during the steady state (rectangular atoms) or during a part of the startup (inclined atoms), spreading the high energy of the fundamental, and hiding the evolutions of the bar breakage components, in all the other parts of the transient. To tackle this unsolved problem in the technical literature, this paper presents a new transform in which the dragon atoms are defined and built, adapting perfectly their shapes to the harmonic trajectories to be detected, no matter how complex the frequency time evolution might be. As a result, the Dragon Transform generates a time-frequency plot in which the evolutions of the FC and the BBH are traced as very thin lines during the whole capture. This facilitates a very precise and complete detection of the faulty harmonics evolutions. Moreover, the paper presents a quantification method which obtains the time evolution of the BBH amplitudes, enabling the diagnosis. The method has proven its capabilities under two different load levels, showing its excellent performance even under low load, when the faulty harmonics evolve really close to the fundamental. It can be concluded that the Dragon Transform is the first transform that allows a complete and very precise detection and amplitude quantification of the BBH evolutions during complex transients as the startups in inverter-fed induction motors.

## References

- [1] J. Tolvanen, Saving energy with variable speed drives, *World Pumps* 2008 (2008) 32 – 33.
- [2] C. Reza, M. D. Islam, S. Mekhilef, A review of reliable and energy efficient direct torque controlled induction motor drives, *Renewable and Sustainable Energy Reviews* 37 (2014) 919 – 932.
- [3] B. Payne, A. Ball, F. Gu, Detection and diagnosis of induction motor faults using statistical measures, *International Journal of COMADEM* 5 (2002) 5–19.
- [4] M. Akar, Detection of rotor bar faults in field oriented controlled induction motors, *Journal of Power Electronics* 12 (2012).
- [5] L. Beneduce, G. Caruso, D. Iannuzzi, F. Maceri, E. Pagano, L. Piegari, Analysis of a structural failure mode arising in cage rotors of induction machines, *Electrical Engineering* 93 (2011) 179–191.
- [6] C. Bruzzese, O. Honorati, E. Santini, Rotor bars breakage in railway traction squirrel cage induction motors and diagnosis by mcsa technique part i : Accurate fault simulations and spectral analyses, in: 5th IEEE International Symposium on Diagnostics for Electric Machines, Power Electronics and Drives (SDEMPED), pp. 1 – 6.
- [7] S. Nandi, H. A. Toliyat, X. Li, Condition monitoring and fault diagnosis of electrical motors – A review, *IEEE Transactions on Energy Conversion* 20 (2005) 719–729.
- [8] J. Pons-Llinares, D. Morinigo-Sotelo, O. Duque, J. Antonino-Daviu, M. Perez-Alonso, Transient detection of close components through the chirplet transform: Rotor faults in inverter-fed induction motors, in: Proceedings, IECON 2014 - 40th Annual Conference of the IEEE Industrial Electronics Society, pp. 3386–3392.
- [9] K. Yahia, A. Cardoso, S. Zouzou, S. Gueddidi, Broken rotor bars diagnosis in an induction motor fed from a frequency converter: experimental research, *Int J Syst Assur Eng Manag* 3 (2012) 40–46.
- [10] W. Thomson, M. Fenger, Current signature analysis to detect induction motor faults, *Industry Applications Magazine*, IEEE 7 (2001) 26–34.
- [11] M. Abd-el-Malek, A. Abdelsalam, O. Hassan, Induction motor broken rotor bar fault location detection through envelope analysis of start-up current using hilbert transform, *Mechanical Systems and Signal Processing* 93 (2017) 332–350.
- [12] B. Sauer, H. Böhm, E. Scharstein, Squirrel cage rotor for an electrical motor, 1993. Germany Patent WO/1994/001918.
- [13] G. Dressel, Electric machine with a squirrel-cage rotor, 2007. US Patent 7215056.
- [14] J. Amezcua-Sanchez, M. Valtierra-Rodriguez, D. Camarena-Martinez, D. Granados-Lieberman, R. Romero-Troncoso, A. Dominguez Gonzalez, Fractal dimension-based approach for detection of multiple combined faults on induction motors, *Journal of Vibration and Control* 22 (2015).
- [15] J. Pons-Llinares, V. Climente-Alarcon, F. Vedreno-Santos, J. Antonino-Daviu, M. Riera-Guasp, Electric machines diagnosis techniques via transient current analysis, in: IECON 2012 - 38th Annual Conference on IEEE Industrial Electronics Society, pp. 3893–3900.
- [16] V. Ghorbanian, J. Faiz, A survey on time and frequency characteristics of induction motors with broken rotor bars in line-start and inverter-fed modes, *Mechanical Systems and Signal Processing* 54-55 (2015) 427 – 456.
- [17] D. Morinigo-Sotelo, L. A. Garcia-Escudero, O. Duque-Perez, M. Perez-Alonso, Practical aspects of mixed-eccentricity detection in pwm voltage-source-inverter-fed induction motors, *IEEE Transactions on Industrial Electronics* 57 (2010) 252–262.

- [18] V. Ghorbanian, J. Faiz, A survey on time and frequency characteristics of induction motors with broken rotor bars in line-start and inverter-fed modes, *Mechanical Systems and Signal Processing* 54-55 (2015) 427–456.
- [19] J. Faiz, V. Ghorbanian, M. Ebrahimi, A survey on condition monitoring and fault diagnosis in line-start and inverter-fed broken bar induction motors, in: *2012 IEEE International Conference on Power Electronics, Drives and Energy Systems (PEDES)*, pp. 1–5.
- [20] J. Pons-Llinares, J. Antonino-Daviu, J. Roger-Folch, D. Morinigo-Sotelo, O. Duque-Perez, Eccentricity diagnosis in inverter - fed induction motors via the analytic wavelet transform of transient currents, in: *The XIX International Conference on Electrical Machines - ICEM 2010*, pp. 1–6.
- [21] T. M. Wolbank, G. Stojicic, P. Nussbaumer, Monitoring of partially broken rotor bars in induction machine drives, in: *IECON 2010 - 36th Annual Conference on IEEE Industrial Electronics Society*, pp. 912–917.
- [22] J. R. Millan-Almaraz, R. J. Romero-Troncoso, R. A. Osornio-Rios, A. Garcia-Perez, Wavelet-based methodology for broken bar detection in induction motors with variable-speed drive, *Electric Power Components and Systems* 39 (2011) 271–287.
- [23] V. Fernandez-Cavero, D. Morinigo-Sotelo, O. Duque-Perez, J. Pons-Llinares, A comparison of techniques for fault detection in inverter-fed induction motors in transient regime, *IEEE Access* 5 (2017) 8048–8063.
- [24] A. Silva, S. Gupta, A. Bazzi, A. Ulatowski, Wavelet-based information filtering for fault diagnosis of electric drive systems in electric ships, *ISA Transactions* 78 (2018) 105–115.
- [25] Y. Liu, A. Bazzi, A review and comparison of fault detection and diagnosis methods for squirrel-cage induction motors: State of the art, *ISA Transactions* 70 (2017) 400–409.
- [26] J. Pons-Llinares, M. Riera-Guasp, J. Antonino-Daviu, T. G. Habetler, Pursuing optimal electric machines transient diagnosis: The adaptive slope transform, *Mechanical Systems and Signal Processing* 80 (2016) 553–569.
- [27] J. Pons-Llinares, J. Antonino-Daviu, J. Roger-Folch, D. Morinigo-Sotelo, O. Duque-Perez, Mixed eccentricity diagnosis in inverter-fed induction motors via the adaptive slope transform of transient stator currents, *Mechanical Systems and Signal Processing* 48 (2014) 423–435.
- [28] S. Mann, S. Haykin, The chirplet transform: A generalization of Gabor's logon transform, *Vision Interface '91* (1991) 205–212. ISSN 0843-803X.
- [29] T. A. Garcia-Calva, D. Morinigo-Sotelo, R. de Jesus Romero-Troncoso, Non-uniform time resampling for diagnosing broken rotor bars in inverter-fed induction motors, *IEEE Transactions on Industrial Electronics* 64 (2017) 2306–2315.
- [30] W. Deleroi, Broken bar in a squirrel-cage rotor of an induction motor – description by superimposed fault-currents, *Archiv fñijr elektrotechnik* 67 (1984) 91–99.
- [31] J. M. Aller, T. G. Habetler, R. G. Harley, R. M. Tallam, Sang Bin Lee, Sensorless speed measurement of ac machines using analytic wavelet transform, *IEEE Transactions on Industry Applications* 38 (2002) 1344–1350.

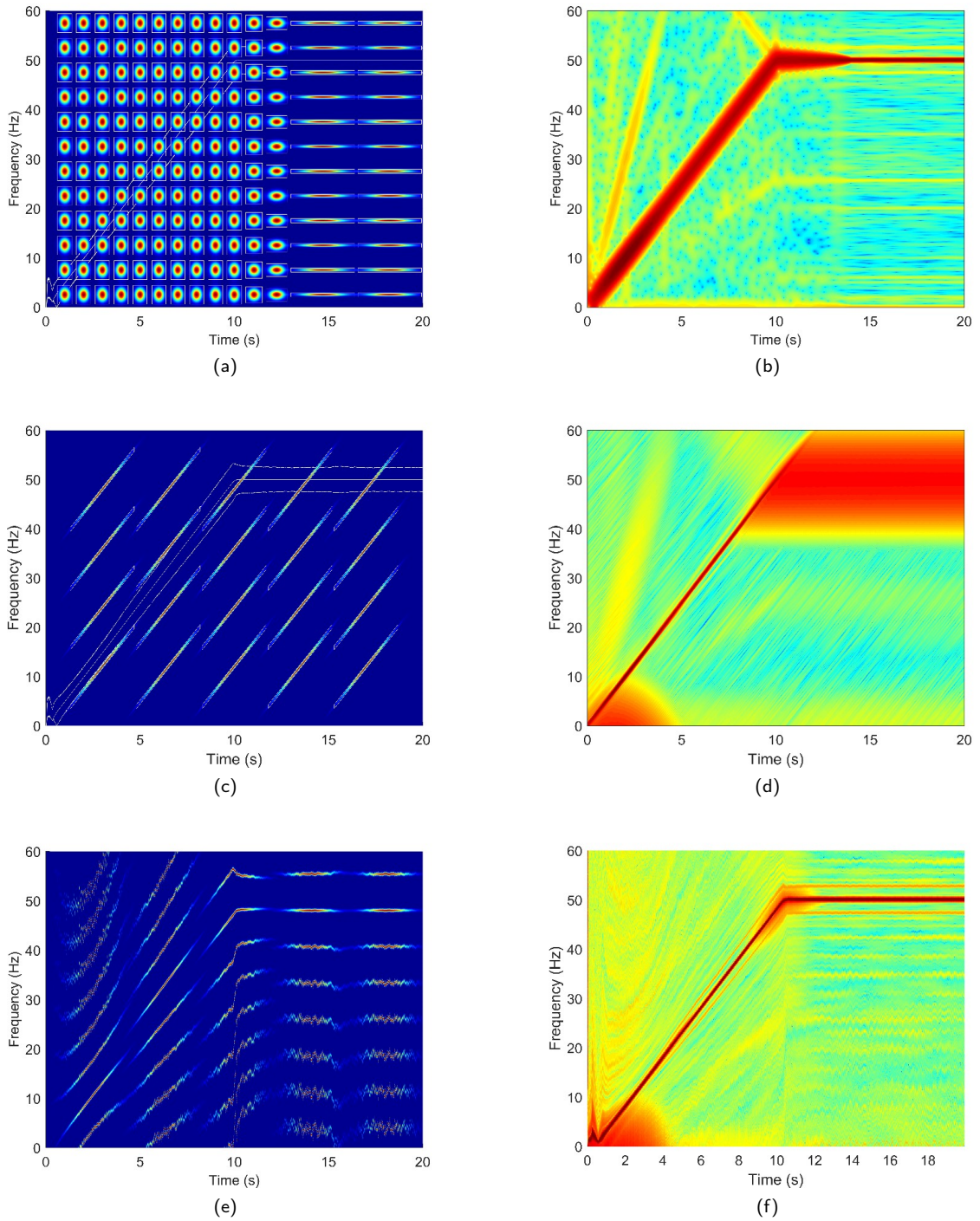


**Figure 11:** Comparison of the atoms family and the transform result for the Adaptive Slope Transform, Chirplet Transform and Dragon Transform.

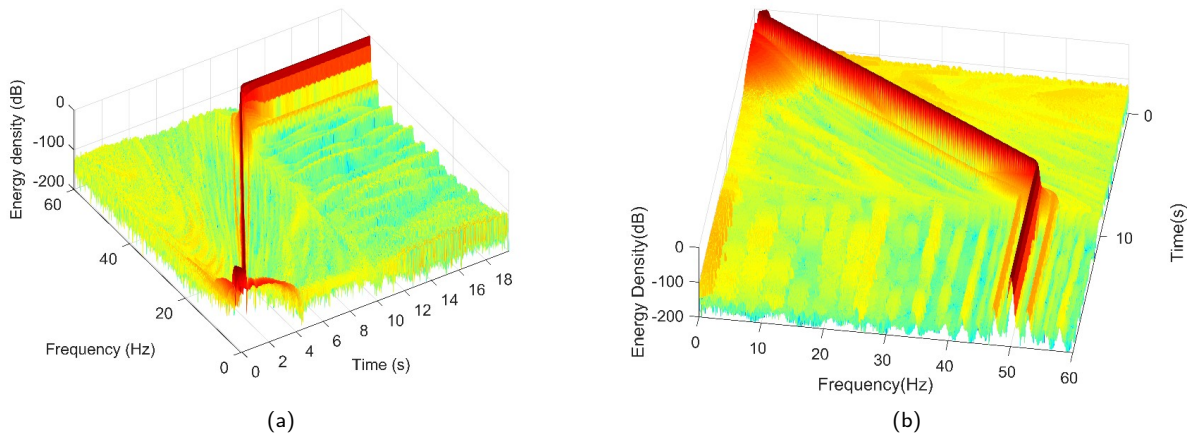


**Figure 12:** 3D views of the DT result when applied to the current of an induction motor with a bar breakage (Fig. 9b).

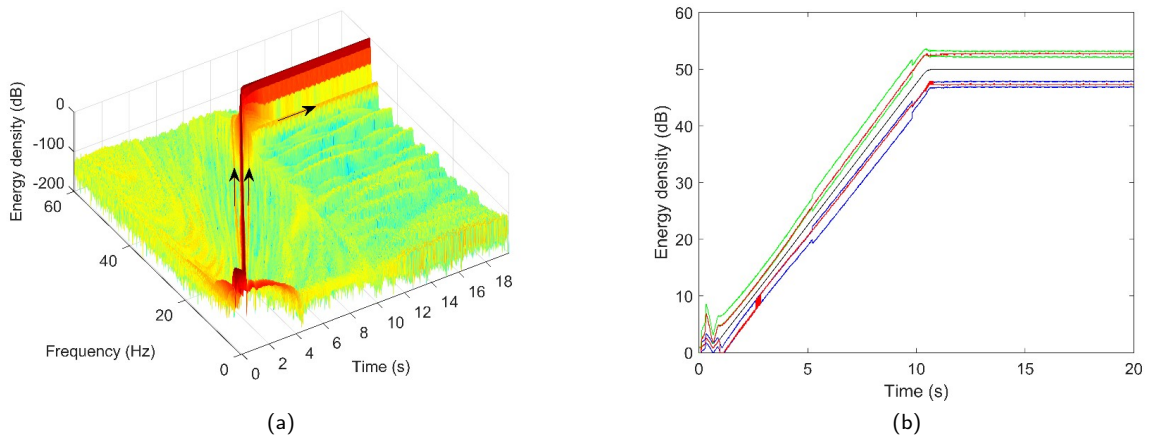


**Figure 13:** (a) 3D view shown in (Fig. 12a) with the BBH trajectories marked with arrows. (b) The FC evolution (black), the frequency bands along the BBH theoretical evolutions (green and blue), and the final BBH evolutions (red).

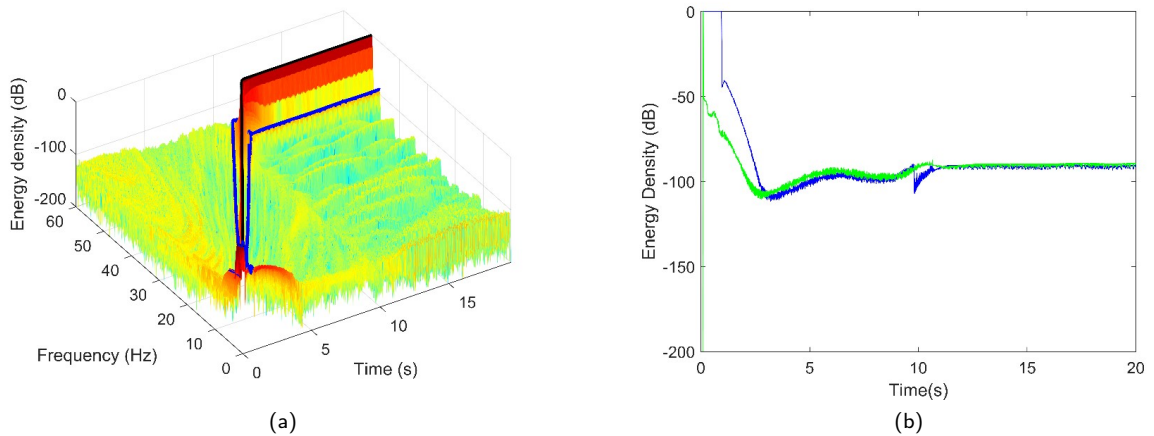


**Figure 14:** (a) 3D view shown in (Fig. 12a) with the final BBH evolutions traced in blue and the FC evolution traced in black. (b) The time evolution of the energy density along the BBH evolutions (blue and green).

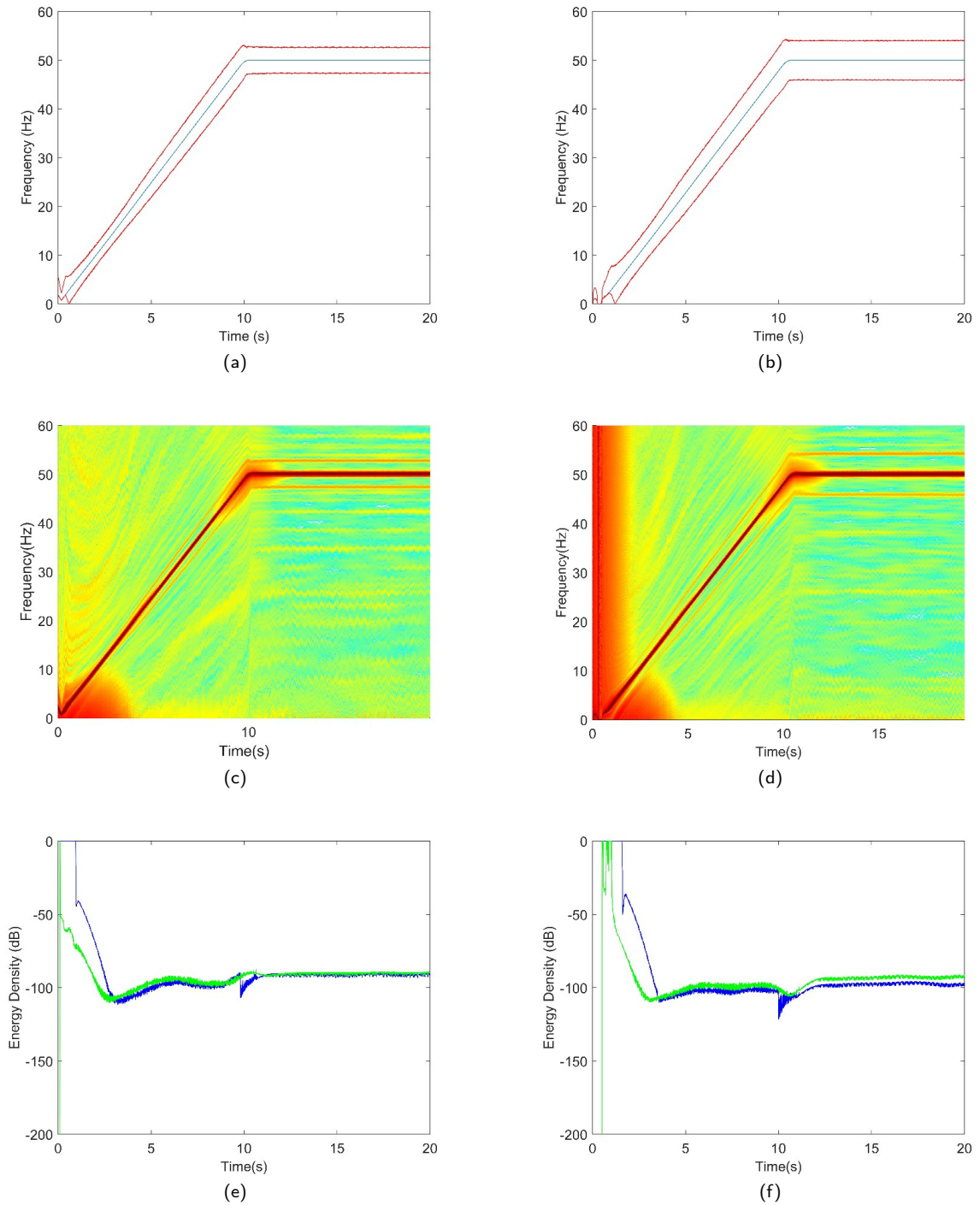


**Figure 15:** Results for the bar breakage motor current under low load (left) and high load (right): evolution (top) of the FC (blue) and BBH (red), Dragon Transform (middle) and quantification (bottom).

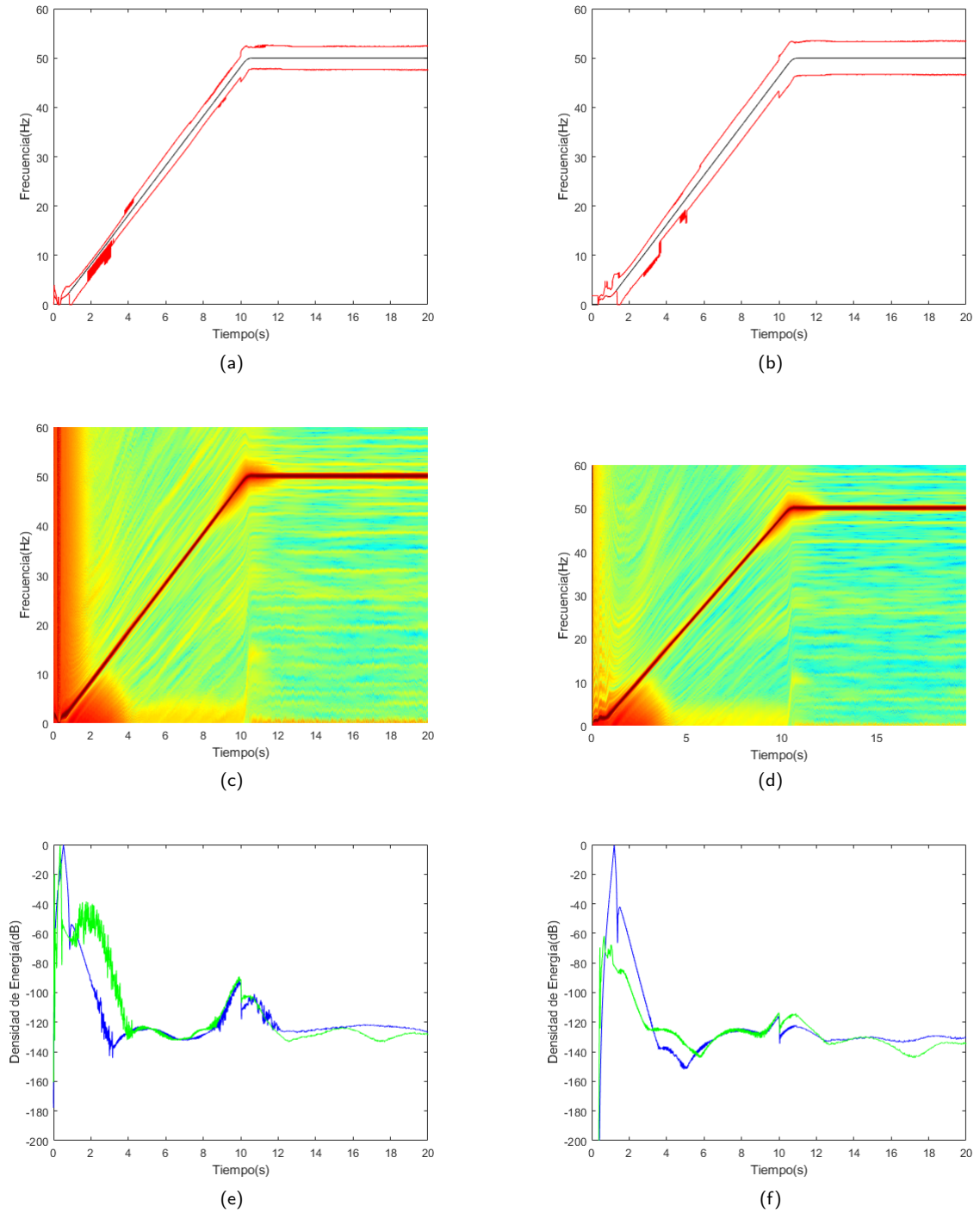


**Figure 16:** Results of the analysis of the current of a healthy motor under low load (left) and high load (right): evolution (top) of the FC (blue) and BBH (red), Dragon Transform (middle) and quantification (bottom).